Mech. Sci., 17, 1105–1119, 2026
https://doi.org/10.5194/ms-17-1105-2026
© Author(s) 2026. This work is distributed under
the Creative Commons Attribution 4.0 License.

mechanical sciences

Research on the control method of a loading device for machine tool accuracy retention testing

Hongqiang Liu[1], Mingsheng Hu[1], Jiapeng Xing[1], Huan Yang[3], Wei Hong[1], Kuo Liu[1,2], and Dongming Guo[1]

[1]School of Mechanical Engineering, Dalian University of Technology, Dalian, 116024, China
[2]Smart Manufacturing Longcheng Laboratory, Changzhou, 213164, China
[3]Liaoning Province Research Institute of Industry and Information Technology, Shenyang, 110001, China

Correspondence: Jiapeng Xing (jpxing99@mail.dlut.edu.cn)

Received: 29 July 2026 – Revised: 10 October 2026 – Accepted: 19 October 2026 – Published: 27 November 2026

Abstract. Accuracy retention testing is an important means of evaluating the ability of machine tools to retain their accuracy. Actively applying dynamic loads to simulate actual cutting loads is a key part of these tests and enables quantitative investigation of their effects on machine tool accuracy. To accommodate the limited installation space inside a machine tool, a compact 3-degree-of-freedom (3-DOF) on-machine loading device based on a Delta parallel mechanism is developed to apply dynamic loads simultaneously in the X, Y, and Z directions to a vertical machining center. To compensate for loading-force deviations caused by spindle thermal deformation, a model predictive control method combining a backpropagation (BP) neural network and a genetic algorithm (GA), termed BP-GA, is proposed. Experiments show that the proposed method reduces force-tracking errors compared with dynamics-based feedforward control and maintains consistent force-tracking accuracy under different operating conditions. Finally, staged on-machine loading tests with simulated cutting forces are conducted to provide a preliminary analysis of changes in machine tool geometric accuracy under dynamic loading.

1 Introduction

Computer numerical control (CNC) machine tools serve as the cornerstone of national industrial development. Machine tool accuracy retention refers to the ability of machine tools to maintain their original accuracy over extended periods under normal operating conditions, which is a key performance indicator for high-end machine tools (Zhao et al., 2016b). Although domestic CNC machine tools have made great progress in recent years, a substantial gap remains between their accuracy retention and that of leading international models (Wang et al., 2019).

Accuracy retention testing is an important approach to studying machine tool accuracy retention. It helps identify degradation mechanisms and characterize the degradation process, providing a basis for improving accuracy retention (Ma et al., 2015; Zhang et al., 2022). Machine tool accuracy degradation results from the long-term interaction of multiple factors, with cutting loads being a key contributor. Loading tests with simulated cutting loads reproduce the loads experienced during service and can accelerate accuracy degradation by increasing the load level. Such tests are therefore an important part of accuracy retention testing. Developing a loading device capable of simulating cutting loads and an accurate control method is essential for these tests.

Considerable research has been conducted on the structural design of machine tool-loading devices. Archenti et al. (2012) developed a loaded double-ball bar (LDBB) to evaluate machine tool accuracy by applying predefined loads between the spindle and the worktable. Xu and Huang (2023) developed a non-contact electromagnetic loading system for measuring the dynamic performance of spindles. Guo et al. (2018a, b) developed a triaxial loading device, a multi-axis loading device, and a multidimensional force-loading device that follows machine motion (Liu et al., 2020). These devices apply forces and moments in multiple degrees of freedom to

three-axis machine tools and provide preliminary evidence of the feasibility of loading during simultaneous five-axis motion. Existing devices can broadly be classified as single-axis or multi-axis loading devices. Single-axis devices apply force in only one direction and cannot adequately simulate multidimensional cutting loads. Multi-axis devices are generally bulky and occupy substantial space, limiting their use in small machine tools.

Research on control methods specifically for on-machine loading devices remains limited. Guo et al. (2018a, b) used a fuzzy proportional-integral (PI) controller for their triaxial loading device and fuzzy proportional-integral-derivative (PID) controllers for their multi-axis and motion-following loading devices (Liu et al., 2020). In related applications, Ding et al. (2022) used improved sliding-mode dynamic matrix control (DMC) to improve the general applicability and robustness of spindle loading systems. Zhao et al. (2020) used modal-space sliding-mode control to address the effects of dynamic coupling between a flexible load and a parallel mechanism on multidimensional force loading. Zhao et al. (2016a) used a decoupling algorithm to address load-induced motion in electric-control loading systems for flight simulators. Lufinka (2023) used dual-axis synchronous control to coordinate loads and synchronize motion in a biaxial loading device. However, effective control methods are still needed to address force deviations caused by thermal deformation during continuous spindle rotation. The resulting temperature rise changes the relative pose of the spindle and loading device, leading to substantial loading-force deviations.

Neural-network-based control methods have shown promise in robotics and force control. Wang et al. (2024) used a multilayer perceptron to learn the inverse kinematic mapping of a space soft robotic manipulator. Zhu et al. (2024) combined an adaptive radial basis function (RBF) neural network with a sliding-mode robust compensator to address modeling uncertainties in collaborative parallel robots. Yang et al. (2024) combined neural-network-based dynamic modeling with distributionally robust model predictive control for trajectory tracking of constrained robotic manipulators. These methods have yet to be widely applied to force control of on-machine loading devices, and effective intelligent compensation strategies for force deviations caused by spindle thermal deformation remain limited.

This study develops a compact 3-degree-of-freedom (DOF) on-machine loading device based on a Delta parallel mechanism for machine tool accuracy retention testing. The device applies dynamic loads simultaneously in the X, Y, and Z directions within the limited space inside a machine tool. Kinematic and dynamic models are established and used to develop a dynamics-based feedforward controller. A BP-GA (backpropagation (BP) neural network and a genetic algorithm (GA)) model predictive control method is then proposed to compensate for loading-force deviations caused by spindle thermal deformation. Comparative control experiments and on-machine loading tests with simulated cutting forces are conducted to validate the device and control method, providing technical support for accuracy retention testing.

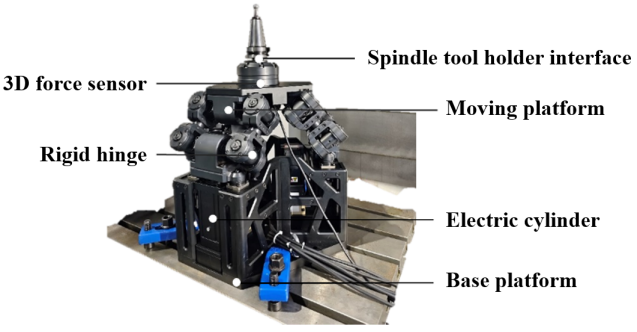

Figure 1. Photograph of the loading device.

2 Development of the loading device based on the Delta parallel mechanism

2.1 Structural design of the device

Under typical machining operations such as turning, milling, and drilling, cutting forces can be resolved into three orthogonal components along the X, Y, and Z axes of the machine tool coordinate system. An on-machine test device for simulating cutting loads must therefore apply forces simultaneously in all three directions.

A Delta parallel mechanism provides three translational degrees of freedom, high structural stiffness, and a compact arrangement of moving components, making it suitable for multidimensional force generation. Conventional Delta mechanisms typically use rotary-actuated limbs, which can result in a large overall envelope and limited load capacity when used inside a machine tool (Feng et al., 2014). Here, high-stiffness electric cylinders replace the actuated revolute joints to reduce the device envelope and increase its load capacity.

The device mainly consists of a base platform, electric cylinders, rigid hinges, a moving platform, a three-dimensional force sensor, and an end effector, as shown in Fig. 1. Its overall dimensions at rest are 442 mm × 392 mm × 437 mm. The compact device can be readily mounted on the worktables of various vertical machining centers.

The device specifications are determined from cutting-load spectra measured during machining and the requirements of accelerated degradation testing. To shorten the test duration without changing the accuracy degradation mechanism, the device must sustain elevated dynamic loads for extended periods (Nelson, 2004). The maximum output force is 2000 N in each of the X, Y, and Z directions; the maximum loading frequency is 25 Hz; and the moving platform has a travel range of ± 5 mm along each axis.

2.2 Control system design of the device

The control system consists of a host computer, a programmable-logic controller (PLC), servo drives, electric cylinders, and a three-dimensional force sensor, as shown in Fig. 2. The host computer generates the desired load signals, executes the control algorithms, and monitors the data. The PLC serves as the lower-level controller and executes motion commands received from the host computer. The servo system drives the electric cylinders, while the force sensor measures the actual output forces at the end effector in real time and feeds them back to the host computer to close the force control loop.

3 Loading control method based on kinematic and dynamic modeling

Output force control of the Delta-based loading device can be developed using forward and inverse kinematics and dynamic modeling of parallel robots (San et al., 2024; Shang et al., 2024). This section first establishes the displacement, velocity, and acceleration relationships among the components. A dynamic model is then derived and used to construct a force controller combining model-based feedforward compensation with force feedback.

3.1 Kinematic analysis and dynamic model

3.1.1 Kinematic analysis

The three limbs of the device are identical in structure and symmetrically distributed, and the structural sketch of a single limb is shown in Fig. 3. Let the center of the base platform be O and the center of the moving platform be P; A_i, B_i, and C_i denote the base connection point, the driving-end connection point, and the moving-platform connection point of the ith ($i = 1, 2, 3$) limb, respectively. R and r are the radial distances from the base and moving-platform connection points to their respective centers, h is the length of the passive arm B_iC_i, l_i is the driving displacement of the ith electric cylinder, and φ_i is the azimuth angle of the ith limb in the base plane.

1. *Inverse kinematics for electric cylinder displacements.*

   According to the closed-loop vector relationship shown in Fig. 3, the ith limb satisfies

   $$\boldsymbol{OA}_i + \boldsymbol{A}_i\boldsymbol{B}_i + \boldsymbol{B}_i\boldsymbol{C}_i + \boldsymbol{C}_i\boldsymbol{P} + \boldsymbol{PO} = 0. \tag{1}$$

   We define $\boldsymbol{OA}_i = R\boldsymbol{t}_i$, $\boldsymbol{A}_i\boldsymbol{B}_i = l_i\boldsymbol{s}_i$, $\boldsymbol{B}_i\boldsymbol{C}_i = h\boldsymbol{e}_i$, $\boldsymbol{PC}_i = r\boldsymbol{t}_i$, and $\boldsymbol{OP} = p$, where $\boldsymbol{t}_i$, $\boldsymbol{s}_i$, and $\boldsymbol{e}_i$ are all unit vectors . Then Eq. (1) can be written as

   $$R\boldsymbol{t}_i + l_i\boldsymbol{s}_i + h\boldsymbol{e}_i - r\boldsymbol{t}_i - p = 0. \tag{2}$$

   According to the geometric relationships shown in Fig. 3, we have

   $$\boldsymbol{t}_i = [\cos\varphi_i, \sin\varphi_i, 0]^{\mathrm{T}}, \tag{3}$$

   $$\boldsymbol{s}_i = [0, 0, 1]^{\mathrm{T}}. \tag{4}$$

   Let the position of the moving-platform center P in the base coordinate system O–xyz be $P(x, y, z)$; then

   $$\boldsymbol{p} = [x, y, z]^{\mathrm{T}}. \tag{5}$$

   Rearranging Eq. (2) gives

   $$h\boldsymbol{e}_i = p - (R - r)\boldsymbol{t}_i - l_i\boldsymbol{s}_i. \tag{6}$$

   Taking the squared norm of both sides of Eq. (6) and using the fact that $\boldsymbol{t}_i$ and $\boldsymbol{s}_i$ are mutually perpendicular, i.e., $\boldsymbol{t}_i^{\mathrm{T}}\boldsymbol{s}_i = 0$, and simplifying, we obtain

   $$l_i^2 - E_i l_i + F_i = 0, \tag{7}$$

   where

   $$E_i = 2\boldsymbol{p}^{\mathrm{T}}\boldsymbol{s}_i, \tag{8}$$

   $$F_i = \boldsymbol{p}^{\mathrm{T}}\boldsymbol{p} + (R - r)^2 - 2(R - r)\boldsymbol{p}^{\mathrm{T}}\boldsymbol{t}_i - h^2. \tag{9}$$

   If the moving-platform position $\boldsymbol{p}$ is known, solving Eq. (7) yields the displacement of each electric cylinder l_i, thereby completing the inverse kinematic solution. Accordingly, the forward kinematic problem can be solved by simultaneously solving the position constraint equations of the three limbs, which is used for moving-platform position calculation and model consistency verification.

2. *Jacobian mapping between the linear velocities of the moving platform and the electric cylinders.*

   Differentiating Eq. (6) with respect to time gives

   $$\dot{\boldsymbol{p}} = \dot{l}_i\boldsymbol{s}_i + h\boldsymbol{\omega}_i \times \boldsymbol{e}_i, \tag{10}$$

   where $\dot{\boldsymbol{p}}$ is the linear velocity of the moving platform, $\dot{l}_i$ is the linear velocity of the ith electric cylinder, and $\boldsymbol{\omega}_i$ is the angular velocity of the ith passive arm. Since the spin of the passive arm about its own axis does not affect the position constraint, only the angular velocity component that changes the direction of the passive arm is considered, i.e., $\boldsymbol{\omega}_i^{\mathrm{T}}\boldsymbol{e}_i = 0$.

   Eliminating $\boldsymbol{\omega}_i$ from the three limbs and combining them into matrix form gives

   $$\mathbf{J}_l\dot{\boldsymbol{l}} = \mathbf{J}_x\dot{\boldsymbol{p}}, \tag{11}$$

   where $\dot{\boldsymbol{l}} = \left[\dot{l_1}, \dot{l_2}, \dot{l_3}\right]^{\mathrm{T}}$ is the electric cylinder velocity vector, $\mathbf{J}_l$ is a diagonal matrix whose diagonal elements are $\boldsymbol{e}_i^{\mathrm{T}}\boldsymbol{s}_i$, and $\mathbf{J}_x$ is obtained by stacking $\boldsymbol{e}_i^{\mathrm{T}}$ row by row. Thus, the inverse Jacobian is $\mathbf{J}_{\mathrm{inv}} = \mathbf{J}_l^{-1}\mathbf{J}_x$, whose ith row is $\boldsymbol{e}_i^{\mathrm{T}}/\boldsymbol{e}_i^{\mathrm{T}}\boldsymbol{s}_i$, and the forward Jacobian is $\mathbf{J}_{\mathrm{fwd}} = \mathbf{J}_{\mathrm{inv}}^{-1}$.

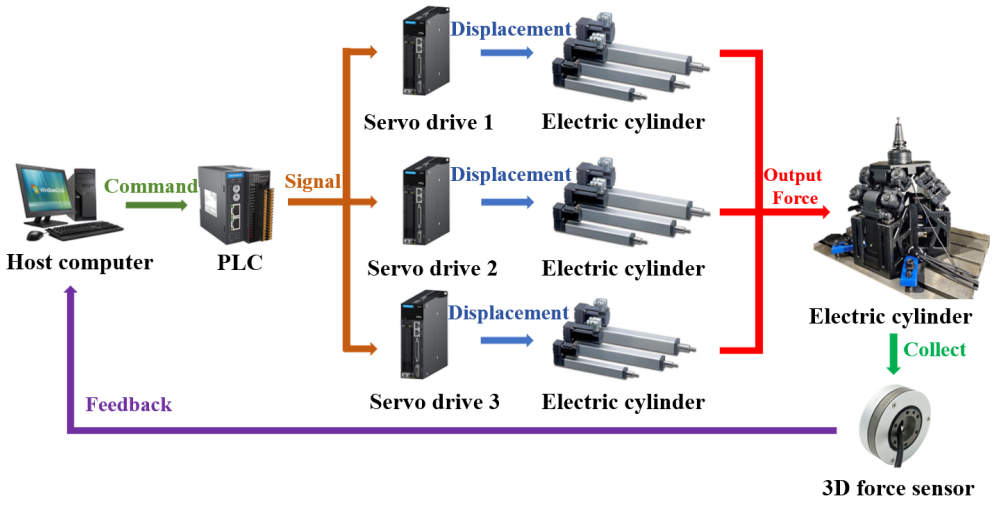

Figure 2. Hardware architecture of the loading-device control system.

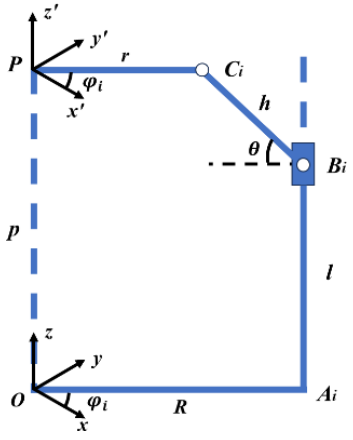

Figure 3. Structural sketch of one limb of the loading device.

3. *Relationships between passive-arm motion and electric-cylinder motion.*

Differentiating Eq. (10) with respect to time and pre-multiplying by $\boldsymbol{e}_i^{\mathrm{T}}$, the acceleration of the moving platform is obtained after rearrangement:

$$\ddot{\boldsymbol{p}} = \mathbf{J}_{\mathrm{fwd}}\ddot{\boldsymbol{l}} - \boldsymbol{U}_l, \boldsymbol{U}_l = h\mathbf{J}_x^{-1}\left[|\omega_1|^2, |\omega_2|^2, |\omega_3|^2\right]^{\mathrm{T}}, \quad (12)$$

where $\ddot{\boldsymbol{l}}$ is the electric-cylinder acceleration vector.

Taking the cross product of $\boldsymbol{e}_i$ with both sides of Eq. (10) and using Eq. (11), the angular velocity of the ith passive arm is obtained:

$$\boldsymbol{\omega}_i = \mathbf{J}_{\omega i}\dot{\boldsymbol{l}}, \quad (13)$$

where $\mathbf{J}_{\omega i} = \frac{1}{h}\tilde{\boldsymbol{e}}_i(\mathbf{J}_{\mathrm{fwd}} - \boldsymbol{s}_i\boldsymbol{q}_i^{\mathrm{T}})$, and $\boldsymbol{q}_i \in \mathbb{R}^3$ is the selection vector for the ith driving component, i.e., $\boldsymbol{q}_1 = [1,0,0]^{\mathrm{T}}$, $\boldsymbol{q}_2 = [0,1,0]^{\mathrm{T}}$, $\boldsymbol{q}_3 = [0,0,1]^{\mathrm{T}}$, and

$$\tilde{\mathbf{e}}_i = \begin{bmatrix} 0 & -e_{iz} & e_{iy} \\ e_{iz} & 0 & -e_{ix} \\ -e_{iy} & e_{ix} & 0 \end{bmatrix}. \quad (14)$$

Differentiating Eq. (10) and taking the cross product with $\boldsymbol{e}_i$, the angular acceleration of the ith passive arm is obtained:

$$\begin{aligned}\boldsymbol{\beta}_i &= \mathbf{J}_{\omega i}\ddot{\boldsymbol{l}} - \boldsymbol{U}_{\beta i}, \boldsymbol{U}_{\beta i} \\ &= \tilde{\mathbf{e}}_i\mathbf{J}_x^{-1}\left[|\omega_1|^2, |\omega_2|^2, |\omega_3|^2\right]^{\mathrm{T}}. \end{aligned} \quad (15)$$

Let G_i be the center of mass of the ith passive arm B_iC_i; since the mass is symmetrically distributed along the rod, G_i is located at the midpoint of B_iC_i. From the midpoint kinematic relationship, the velocity and acceleration of the center of mass are

$$\boldsymbol{v}_i = \mathbf{J}_{vi}\dot{\boldsymbol{l}}, \mathbf{J}_{vi} = \frac{1}{2}\left(\mathbf{J}_{\mathrm{fwd}} + \boldsymbol{s}_i\boldsymbol{q}_i^{\mathrm{T}}\right), \quad (16)$$

$$\begin{aligned}\boldsymbol{a}_i &= \mathbf{J}_{ai}\ddot{\boldsymbol{l}} - \boldsymbol{U}_{ai}, \mathbf{J}_{ai} = \frac{1}{2}\left(\mathbf{J}_{\mathrm{fwd}} + \boldsymbol{s}_i\boldsymbol{q}_i^{\mathrm{T}}\right) \\ &= \mathbf{J}_{vi}, \boldsymbol{U}_{ai} = \frac{1}{2}\boldsymbol{U}_l. \end{aligned} \quad (17)$$

Equations (12)–(17) relate the angular velocities and accelerations of the passive arms and the velocities and accelerations of their centers of mass to the electric-cylinder velocities and accelerations. These relationships form the kinematic basis of the dynamic model.

3.1.2 Dynamic analysis

The system dynamic model is derived using the principle of virtual work. For an ideal system, the total virtual work of the

applied, constraint, and inertial forces is zero for any admissible virtual displacement (Zhai et al., 2024). Accounting for the motor shaft assemblies, electric-cylinder pushrods, passive arms, and moving platform gives

$$\delta W = \boldsymbol{\delta x}_{\mathrm{M}}^{\mathrm{T}} \boldsymbol{N} + \boldsymbol{\delta x}_{l}^{\mathrm{T}} \boldsymbol{F}_{l} + \sum_{i=1}^{3} \boldsymbol{\delta x}_{i}^{\mathrm{T}} \boldsymbol{F}_{i} + \boldsymbol{\delta x}_{p}^{\mathrm{T}} \boldsymbol{F}_{\mathrm{p}} = 0, \quad (18)$$

where δW is the total virtual work of the system; $\boldsymbol{\delta x}_{M}$, $\boldsymbol{\delta x}_{l}$, $\boldsymbol{\delta x}_{i}$, and $\boldsymbol{\delta x}_{p}$ are the virtual displacements of the motor rotor, the electric-cylinder pushrod, the ith passive arm, and the moving platform, respectively; and $\boldsymbol{N}$, $\boldsymbol{F}_{l}$, $\boldsymbol{F}_{i}$, and $\boldsymbol{F}_{p}$ are the resultant external forces (moments) acting on the motor shaft system, the electric-cylinder pushrod, the passive arm, and the moving platform, respectively.

1. *Force analysis of the active arms (electric-cylinder pushrods).*

   The electric-cylinder pushrods undergo translation only and therefore have no rotational inertial torque. Combining the forces acting on the three pushrods gives

   $$\boldsymbol{F}_{l} = m_{l}(\mathbf{s}\mathbf{g} - \ddot{\boldsymbol{l}}), \quad (19)$$

   where m_l is the mass of the electric-cylinder pushrod, $\mathbf{g}$ is the gravitational acceleration vector (vertically downward), and $\mathbf{s}$ is the matrix formed by stacking the unit vectors $\boldsymbol{s}_{i}^{\mathrm{T}}$ row by row.

2. *Force analysis of the passive arms.*

   The passive arms translate and rotate simultaneously. Taking the center of mass G_i as the moment reference point, the external forces (moments) and inertial forces (moments) of the ith passive arm in the base platform coordinate system are

   $$\boldsymbol{F}_{i} = \begin{bmatrix} \boldsymbol{f}_{i} \\ \boldsymbol{n}_{i} \end{bmatrix} = \begin{bmatrix} m_{i}\mathbf{g} - m_{i}\boldsymbol{a}_{i} \\ -{}^{o}\mathbf{I}_{i}\boldsymbol{\beta}_{i} - \boldsymbol{\omega}_{i} \times ({}^{o}\mathbf{I}_{i}\boldsymbol{\omega}_{i}) \end{bmatrix}, \quad (20)$$

   $${}^{o}\mathbf{I}_{i} = {}^{o}\mathbf{R}_{i}^{i}\mathbf{I}_{i}^{o}\mathbf{R}_{i}^{\mathrm{T}} + m_{i}\left(\boldsymbol{P}_{i}^{\mathrm{T}}\boldsymbol{P}_{i}\mathbf{E}_{3} - \boldsymbol{P}_{i}\boldsymbol{P}_{i}^{\mathrm{T}}\right), \quad (21)$$

   where m_i is the mass of the ith passive arm, $\boldsymbol{a}_i$ is the linear acceleration of the ith passive arm, ${}^{o}\mathbf{I}_{i}$ is the inertia tensor of the ith passive arm in the base platform coordinate system, ${}^{i}\mathbf{I}_{i}$ is the inertia tensor of the ith passive arm in its own coordinate system, ${}^{o}\mathbf{R}_{i}$ is the rotation matrix, $\boldsymbol{P}_{i}$ is the position vector of the center of mass G_i of the ith passive arm in the base coordinate system, and $\mathbf{E}_3$ is the 3×3 identity matrix.

3. *Force analysis of the moving platform.*

   In the base platform coordinate system, the external force and moment acting on the centroid of the moving platform are expressed as

   $$\boldsymbol{F}_{p} = \begin{bmatrix} \boldsymbol{f}_{p} \\ \boldsymbol{n}_{p} \end{bmatrix} = \begin{bmatrix} \boldsymbol{f}_{e} + m_{\mathrm{p}}\mathbf{g} - m_{\mathrm{p}}\ddot{\boldsymbol{p}} \\ \boldsymbol{n}_{e} - {}^{o}\mathbf{I}_{p}\boldsymbol{\beta}_{p} - \boldsymbol{\omega}_{p} \times \left({}^{o}\mathbf{I}_{p}\boldsymbol{\omega}_{p}\right) \end{bmatrix}. \quad (22)$$

   Owing to the structural characteristics of the loading device, the moving platform can only translate and cannot rotate in three-dimensional space; hence $\boldsymbol{n}_{p} = \boldsymbol{n}_{e}$ where $\mathbf{f}_{e}$ is the external force acting on the center of the moving platform, m_{p} is the mass of the moving platform, and $\boldsymbol{n}_{\mathrm{e}}$ is the external moment acting on the center of the moving platform; the remaining terms are zero.

4. *Force analysis of the motor shaft assemblies.*

   The external moment and inertial moment acting on the ith motor shaft system are

   $$N_{i} = \tau_{i} - (I_{M} + I_{C} + I_{D})\beta_{Mi}, \quad (23)$$

   where τ_i is the input torque of the ith motor; β_{Mi} is the angular acceleration of the ith motor; and I_M, I_C, and I_D are the moments of inertia of the motor rotor, the coupling, and the lead screw assembly, respectively.

   The relationships between the virtual displacements of the passive arm, the moving platform, and the motor rotor and the virtual displacement of the electric cylinder pushrod are, respectively,

   $$\boldsymbol{\delta x}_{i}^{\mathrm{T}} = \boldsymbol{\delta x}_{1}^{\mathrm{T}} \begin{bmatrix} \mathbf{J}_{\mathrm{vi}} \\ \mathbf{J}_{\omega i} \end{bmatrix}^{\mathrm{T}}, \quad \boldsymbol{\delta x}_{\mathrm{p}}^{\mathrm{T}} = \boldsymbol{\delta x}_{1}^{\mathrm{T}} \mathbf{J}_{\mathrm{fwd}}^{\mathrm{T}},$$
   $$\boldsymbol{\delta x}_{M}^{\mathrm{T}} = \frac{2\pi}{p_{\mathrm{s}}} \boldsymbol{\delta x}_{l}^{\mathrm{T}}. \quad (24)$$

   Substituting Eqs. (23) and (24) into Eq. (18) and simplifying, the motor input torque is obtained:

   $$\boldsymbol{\tau} = \frac{p_{\mathrm{s}}}{2\pi} \left(-\boldsymbol{F}_{l} - \sum_{i=1}^{3} \begin{bmatrix} \mathbf{J}_{vi} \\ \mathbf{J}_{\omega i} \end{bmatrix}^{\mathrm{T}} \boldsymbol{F}_{i} - \mathbf{J}_{\mathrm{fwd}}^{\mathrm{T}} \boldsymbol{F}_{\mathrm{p}} \right) + I_{MCD}\boldsymbol{\beta}_{M}, \quad (25)$$

   where $I_{MCD} = I_M + I_C + I_D$ is the total moment of inertia of the motor shaft system, and $\boldsymbol{\beta}_{M}$ is the motor angular acceleration vector.

   Substituting Eqs. (19), (20), and (22) into Eq. (25) and collecting the acceleration-dependent, velocity-dependent, and constant terms gives the standard dynamic model:

   $$\boldsymbol{\tau} = \mathbf{M}(\boldsymbol{l})\ddot{\boldsymbol{l}} + \mathbf{V}(\boldsymbol{l}, \dot{\boldsymbol{l}})\dot{\boldsymbol{l}} + \mathbf{G}(\boldsymbol{l}) + \mathbf{D}(\boldsymbol{l}), \quad (26)$$

   where $\mathbf{M}(\boldsymbol{l})$ is the inertia term, $\mathbf{V}(\boldsymbol{l}, \dot{\boldsymbol{l}})$ is the velocity term, $\mathbf{G}(\boldsymbol{l})$ is the gravity term, and $\mathbf{D}(\boldsymbol{l})$ is the load term.

3.2 Controller design

Using the dynamic model established in Sect. 3.1.2 for feedforward compensation, a model-based force controller is

constructed, as shown in Fig. 4. The controller takes the desired three-directional forces as input; the corresponding electric cylinder displacement commands are obtained by solving the kinematic and dynamic models and are sent by the PLC to the electric cylinders for execution. The three-dimensional force sensor collects the actual output forces in real time; after comparison with the desired forces, a displacement correction is generated through the force-feedback correction stage and superimposed on the displacement commands, forming a closed-loop force control combining feedforward compensation and force feedback.

4 Neural-network-based loading control method

The loading device is connected to the machine tool spindle through a tool holder. Prolonged high-speed spindle rotation causes a temperature rise and thermal deformation, resulting in deviations between the actual and desired output forces. The dynamics-based feedforward method in Sect. 3 cannot adequately compensate for these deviations. This section therefore proposes BP-GA model predictive control. A BP neural network models the nonlinear mapping from the three electric cylinder displacements to the three loading-force components. The displacements are the control variables, and the force components are the predicted outputs. A genetic algorithm solves the receding-horizon optimization problem online, while force feedback corrects the initial predicted output to compensate for force deviations caused by spindle thermal deformation.

4.1 Development of BP neural network

First, the controller constructed in Sect. 3 is used to drive the loading device to preload the machine tool so as to collect a dataset. The three electric cylinders perform synchronous sinusoidal motion, with displacement commands of $q_1 = A_\mathrm{d}\sin(2\pi f t)$ and $q_2 = q_3 = -A_\mathrm{d}\sin(2\pi f t)$, respectively, and the motion frequency of the electric cylinders f is 25 Hz; the displacement amplitude A_d starts from 0.10 mm and increases by 0.05 mm every day for 7 d, with continuous operation for 8 h each day. The three electric cylinder displacements and the three-dimensional force are synchronously recorded at a sampling frequency of 1000 Hz; 20 complete steady-state cycles are uniformly selected every hour, and 20 points are sampled at equal intervals in each cycle, yielding a total of 22 400 samples. In chronological order, the samples from the first 70 % of each day's duration are taken as the training set, and those from the latter 30 % are taken as the test set, with the three electric cylinder displacements as inputs and the X-, Y-, and Z-directional forces measured by the sensor as outputs.

The collected electric cylinder displacements range approximately from ± 0.10 to ± 0.4 mm, and the three-dimensional forces range approximately from 500 to 2000 N. Because the features have different units and numerical ranges, the min–max method is used to linearly normalize each feature to [0, 1] so as to eliminate the effects of different units and improve the generalization ability. The normalization is calculated as in Eq. (27):

$$x_\mathrm{norm} = \frac{x - x_\mathrm{min}}{x_\mathrm{max} - x_\mathrm{min}}, \tag{27}$$

where x is the original feature value; x_max and x_min are the maximum and minimum values of this feature in the training set, respectively; and x_norm is the normalized result.

The BP neural network is simple in structure and easy to implement, and it has a strong approximation capability for static nonlinear mappings such as displacement force; it has been widely used in robot modeling and control and is therefore selected as the prediction model (Ma et al., 2024). The network adopts one input layer, one hidden layer, and one output layer: the input layer contains three nodes corresponding to the three electric cylinder displacements; the output layer contains three nodes corresponding to the three-directional output forces and adopts a linear activation function; the number of hidden-layer neurons is determined to be 10 through comparison of training results; the sigmoid function, which is smooth and differentiable and facilitates error backpropagation, is selected as the hidden-layer activation function. The network takes the mean squared error (MSE) as the loss function, and the conjugate gradient method is used to iteratively optimize the weights and biases of each layer; this method conjugately combines the current gradient with the previous search directions and requires only first-order derivative information, with convergence speed and numerical stability superior to standard gradient descent (Sato et al., 2024). The initial weights and biases are randomly generated, the learning rate is set to 0.01, the maximum number of training iterations is set to 3500, and the network topology is shown in Fig. 5.

The training loss is plotted against the number of iterations in Fig. 6. The loss decreases and approaches a stable value, indicating convergence of the network.

The trained BP neural network is evaluated on the test set. Figure 7 compares the predicted and measured values, showing no evident overfitting or underfitting. Table 1 presents quantitative performance metrics: root mean square error (RMSE), mean absolute error (MAE), and the coefficient of determination (R^2). The R^2 values exceed 0.99 in all three directions, indicating good regression accuracy on unseen samples and supporting the use of the network as the model predictive control (MPC) prediction model.

4.2 BP-GA model predictive control

Model predictive control (MPC) uses a prediction model, the current system state, and candidate control inputs to predict system outputs. It determines the optimal control input through online receding-horizon optimization and corrects the initial predicted output using measured output feed-

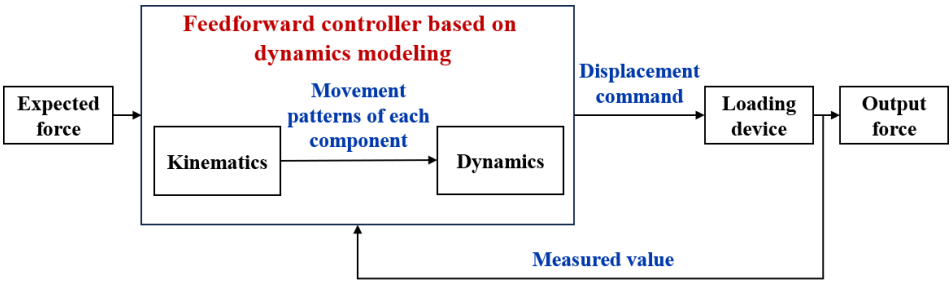

Figure 4. Feedforward controller based on dynamics modeling.

Table 1. BP neural network prediction accuracy for the three force components.

Output direction	RMSE (N)	Relative RMSE (%)	MAE (N)	Relative MAE (%)	R^2
X	93.2	5.10	84.3	4.61	0.994
Y	102.0	5.85	93.3	5.35	0.993
Z	111.9	5.36	104.8	5.02	0.991

Note that RMSE=$\sqrt{\frac{1}{N}\sum_{i=1}^{N}(F_{\mathrm{p},i}-F_{\mathrm{t},i})^2}$, MAE=$\frac{1}{N}\sum_{i=1}^{N}|F_{\mathrm{p},i}-F_{\mathrm{t},i}|$, $R^2=1-\frac{\sum_{i=1}^{N}(F_{\mathrm{p},i}-F_{\mathrm{t},i})^2}{\sum_{i=1}^{N}(F_{\mathrm{t},i}-\overline{F}_{\mathrm{t}})^2}$, where N is the total number of sampling points in the test set, $F_{\mathrm{t},i}$ is the measured output force at the ith sampling point, $F_{\mathrm{p},i}$ is the output force predicted by the BP neural network, and $\overline{F}_{\mathrm{t}}$ is the mean value of the measured output forces; the measured and predicted forces and the mean measured force are expressed in N. The relative RMSE = RMSE/$F_{\max}\times 100\,\%$, and the relative MAE = MAE/$F_{\max}\times 100\,\%$, where $F_{\max}$ is the peak value (absolute maximum) of the measured output forces in the test set in the corresponding direction, which is approximately 1827, 1744, and 2089 N in the X, Y, and Z directions, respectively.

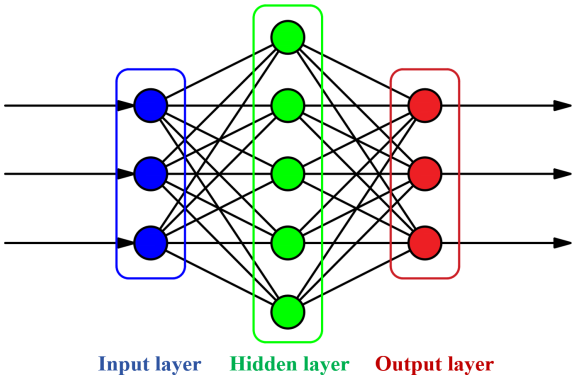

Figure 5. BP neural network structure.

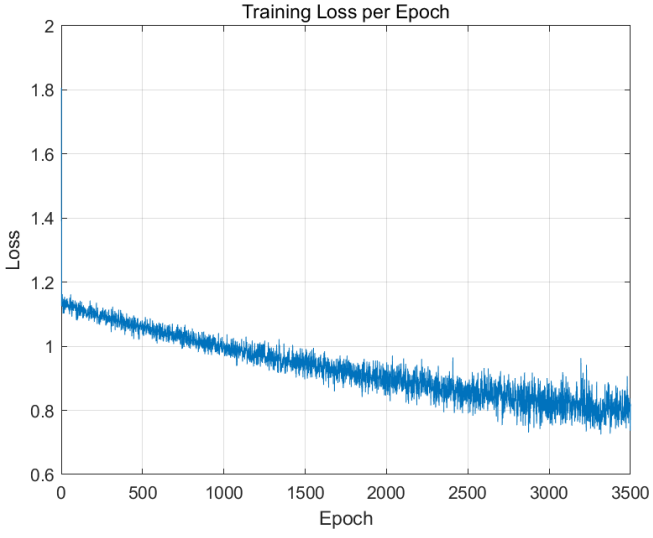

Figure 6. Neural network loss function.

back. Prediction, receding-horizon optimization, and feedback correction are its three basic components. The BP neural network developed in Sect. 4.1 serves as the prediction model, and a genetic algorithm performs the online optimization. Genetic algorithms do not require a continuously differentiable objective function and use population-based searches with global search capability. A genetic algorithm is therefore selected for the non-convex, non-differentiable optimization problem described for the BP prediction model (Cavus and Allahham, 2024). The control procedure is as follows.

Step 1. A random-number tool is used to generate binary strings with a population size of P, range $[-a, a]$, and length L as the initial population. In this paper, the population size is set to $P = 100$, with an independent population corresponding to each electric cylinder, and the binary word length of an individual is $L = 10$; after the binary strings are decoded into real-valued displacements, they become the candidate electric cylinder displacements, and the single-step displacement range is set to $[-0.10, 0.10]$ mm.

Step 2. Decode the population members into candidate displacements and use the BP neural network to predict the cor-

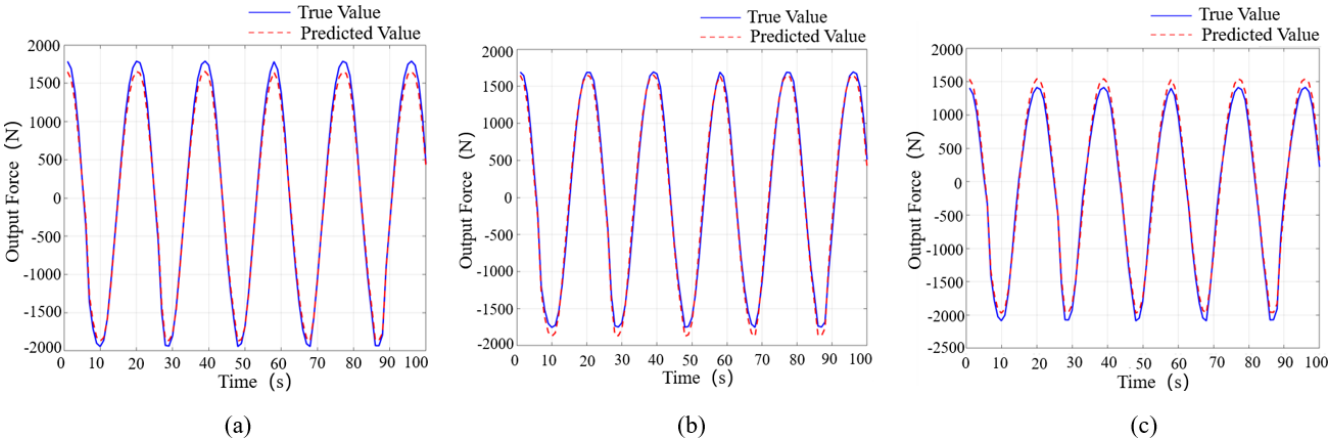

Figure 7. Validation of the predicted results against the true values. **(a)** Output force in the X direction. **(b)** Output force in the Y direction. **(c)** Output force in the Z direction.

responding forces in the X, Y, and Z directions. Evaluate the objective in Eq. (28) using the predicted and desired forces, and use it to calculate fitness.

$$J = \sum_{i=1}^{3} \left[(y_{\mathrm{pi}} - y_{\mathrm{di}})^2 + \lambda {l_i}^2 \right], l_i = [-b, b] \tag{28}$$

In the above, y_{pi} and y_{di} are the predicted and desired values of the ith directional loading force, respectively; l_i is the candidate electric cylinder displacement; $b = 0.10$ mm; and λ is the displacement penalty weight (set to $\lambda = 1$). The first term is the sum of the squared three-directional force-tracking errors, and the second term is the displacement penalty used to suppress an excessively large single-step displacement. The genetic algorithm takes the minimization of J as the optimization objective, with the fitness set to fitvalue $= 1/J$, and performs roulette wheel selection in proportion to fitness.

Step 3. Roulette wheel selection is adopted in proportion to fitness, with a crossover probability $P_{\mathrm{c}} = 0.80$ and a mutation probability $P_{\mathrm{m}} = 0.10$; crossover exchanges part of the binary strings of two individuals at random positions, and mutation randomly flips a certain bit of an individual with a small probability, thereby producing a new population.

Step 4. The fitness of the new population is recalculated, and steps 1–3 are repeated until the maximum number of evolutionary generations (50) is reached or the optimal fitness shows no obvious improvement for five consecutive generations; the optimal individual is decoded into the displacement command for the current control cycle.

Step 5. Apply only the optimal displacement command obtained for the current control cycle. In the next cycle, update the initial predicted output using the forces measured by the three-dimensional force sensor, appropriately expand the candidate displacement range, and repeat the optimization. The control (optimization) period is 50 ms, and the inner servo position loop runs at a period of 1 ms. Figure 8 presents the algorithm flowchart, and Table 2 lists its key parameters.

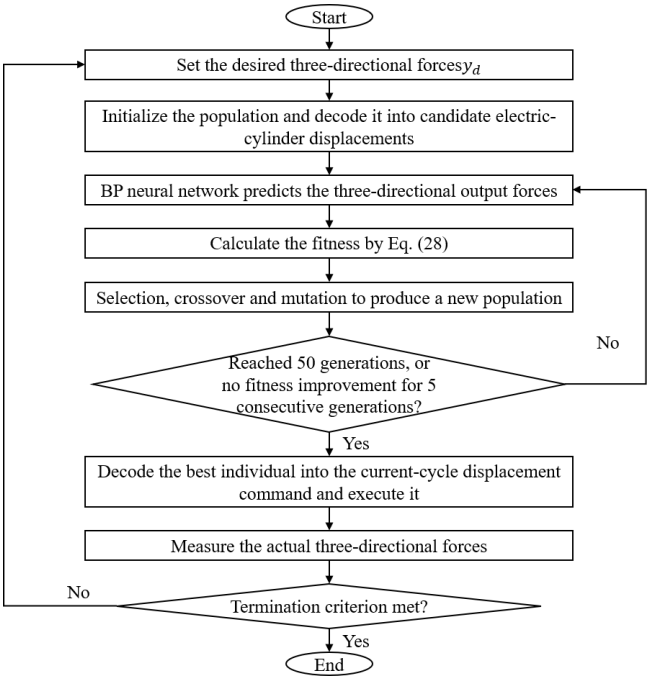

Figure 8. Flowchart of BP-GA model predictive control.

4.3 Model predictive controller design

The BP-GA model predictive controller combines the BP neural network prediction model in Sect. 4.1, online genetic algorithm optimization in Sect. 4.2, and force feedback correction. Its structure is shown in Fig. 9.

The desired forces in the X, Y, and Z directions are the controller inputs. During each control cycle, the genetic algorithm generates candidate displacements, and the BP neural network predicts the corresponding output forces. Iterative optimization of Eq. (28) yields the optimal displacement commands, which are sent to the PLC to drive the electric

Table 2. Parameter settings of the BP-GA model predictive controller.

Parameter	Value
Prediction horizon N_p/control horizon N_c	1 ($N_p = N_c = 1$, single-step receding-horizon optimization)
Control (optimization) period	50 ms
Servo position inner-loop period	1 ms
Decision variables	Candidate displacements $\boldsymbol{l}$ of the three electric cylinders
Encoding method	Binary encoding, with a word length of 10 bits for each electric cylinder
Population size	100 (an independent population for each of the three electric cylinders)
Single-step displacement search range	$[-0.10, 0.10]$ mm
Selection/crossover/mutation	Roulette wheel selection; crossover rate 0.80; mutation rate 0.10
Termination condition	Maximum 50 evolutionary generations or no improvement of the optimal value for 5 consecutive generations
Average computation time per period	Approximately 38 ms

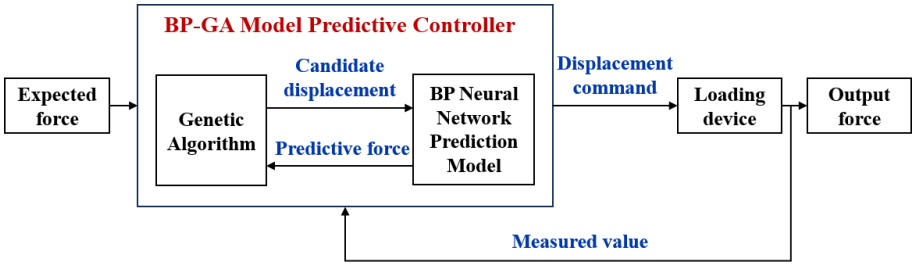

Figure 9. Structure of the BP-GA model predictive controller.

cylinders. The measured output forces are fed back to correct the initial predicted output in the next cycle. Repeating this process compensates online for force deviations caused by spindle thermal deformation and other factors, enabling accurate control of all three force components.

5 Validation of the control method and on-machine loading test of the machine tool

5.1 Comparative validation of the control methods

To evaluate the proposed BP-GA model predictive control method, comparative experiments are conducted against dynamics-based feedforward control. A three-axis vertical machining center is used, with the loading device connected to the spindle through a tool holder, as shown in Fig. 10.

Let the desired output forces of the loading device in the X, Y, and Z directions be $Fj = A\sin(2\pi ft)(j \in \{X, Y, Z\})$, where A is the loading-force amplitude, f is the loading frequency, and t is time. In the test, the amplitudes of the three-directional loading forces are all set to 1500 N, the loading frequency is 5 Hz, the spindle speed is maintained at 4000 r min^{-1}, and loading continues for 2 h.

During the test, an infrared thermal imager records the machine tool temperature field, as shown in Fig. 11. The temperature rises from approximately 18 °C to approximately 29 °C. The resulting spindle thermal deformation changes the relative position of the loading device and spindle, causing deviations between the actual and desired output forces.

First, the feedforward controller described in Sect. 3.2 is used to control the loading device. The measured output forces and spindle end temperature are plotted in Fig. 12a–c.

With dynamics-based feedforward control, the deviations of the mean X-, Y-, and Z-direction forces from their desired means at the start of loading are 50, 170, and 150 N, respectively, as shown in Fig. 12a–c. As spindle temperature and thermal deformation increase, the mean force deviation remains approximately 30–50 N in X and approximately 180 N in Y, with little dependence on temperature. The mean Z-direction force is more sensitive to spindle thermal deformation: its deviation increases with temperature, reaching approximately 630 N at thermal equilibrium.

The BP-GA model predictive controller described in Sect. 4.3 is then used to compensate for the large force deviations caused by spindle thermal deformation. The measured temperature and force data are shown in Fig. 12d–f.

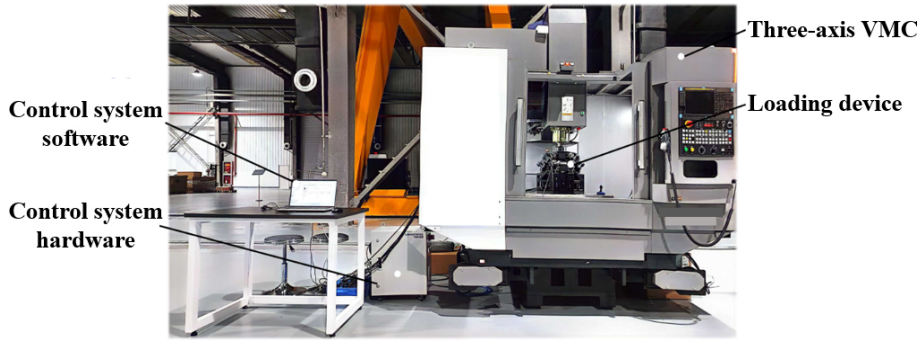

Figure 10. Experimental setup for the on-machine loading control test.

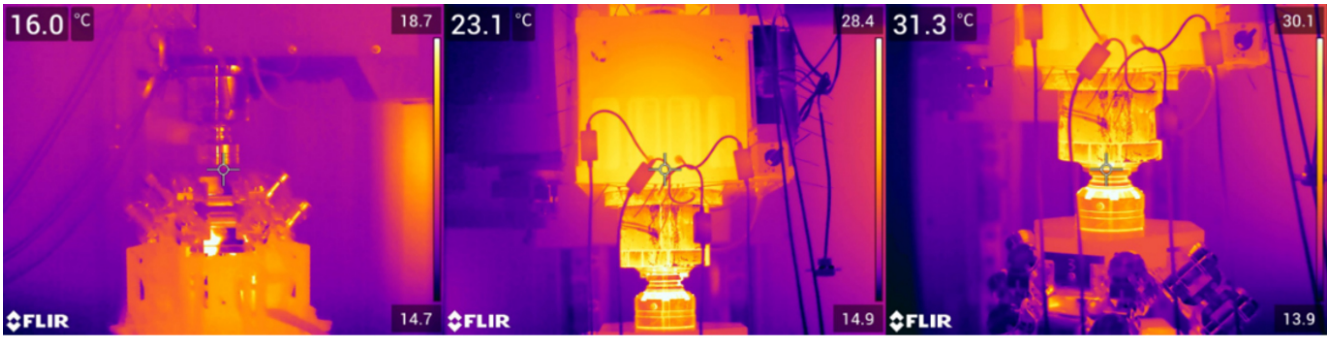

(a) (b) (c)

Figure 11. Evolution of the machine tool temperature field. **(a)** Spindle stationary. **(b)** Spindle during temperature rise. **(c)** Spindle at thermal equilibrium.

With BP-GA model predictive control, the mean force deviations at the start of loading are approximately 20, 25, and 65 N in X, Y, and Z, respectively. At thermal equilibrium, they are approximately 45, 55, and 250 N. The X-direction mean force deviation is approximately 20–50 N under both methods, with no substantial difference. In Y, BP-GA reduces the deviation from approximately 170 to 25 N at the start of loading, a reduction of about 85 %, and from approximately 180 to 55 N at thermal equilibrium, a reduction of about 70 %. In Z, it reduces the deviation from approximately 150 to 65 N initially, a reduction of about 56 %, and from approximately 630 to 250 N at thermal equilibrium, a reduction of about 60 %. These results indicate that BP-GA model predictive control effectively compensates for loading-force errors associated with spindle thermal deformation.

Further experiments assess force-tracking accuracy and performance across operating conditions using dynamics-based feedforward control as the baseline. One operating parameter is varied at a time over loading frequencies of 5–15 Hz, force amplitudes of 500–2000 N, and spindle speeds of 2000–6000 r min^{-1}. Table 3 reports the force-tracking RMSE in N. The errors are evaluated over complete steady-state loading cycles, excluding startup and shutdown transients, using force signals sampled at 1000 Hz.

Table 3 shows that the force-tracking RMSE of dynamics-based feedforward control depends markedly on force amplitude, loading frequency, and spindle speed. Its RMSE generally increases in all three directions as loading frequency increases, indicating more pronounced dynamic response errors at higher frequencies. Spindle speed has a stronger effect on the Z-direction tracking error, consistently with greater spindle heating and axial thermal deformation. BP-GA model predictive control maintains lower RMSE values in all three directions across the tested conditions, with generally smaller variations between conditions. Under most conditions, it reduces RMSE by approximately 30 %–70 % relative to dynamics-based feedforward control, indicating good tracking accuracy and adaptability to changes in amplitude, frequency, and spindle speed.

5.2 On-machine loading test of the machine tool with simulated cutting forces

An on-machine loading test with simulated cutting forces is conducted on a domestically manufactured three-axis vertical machining center of a certain model to validate the de-

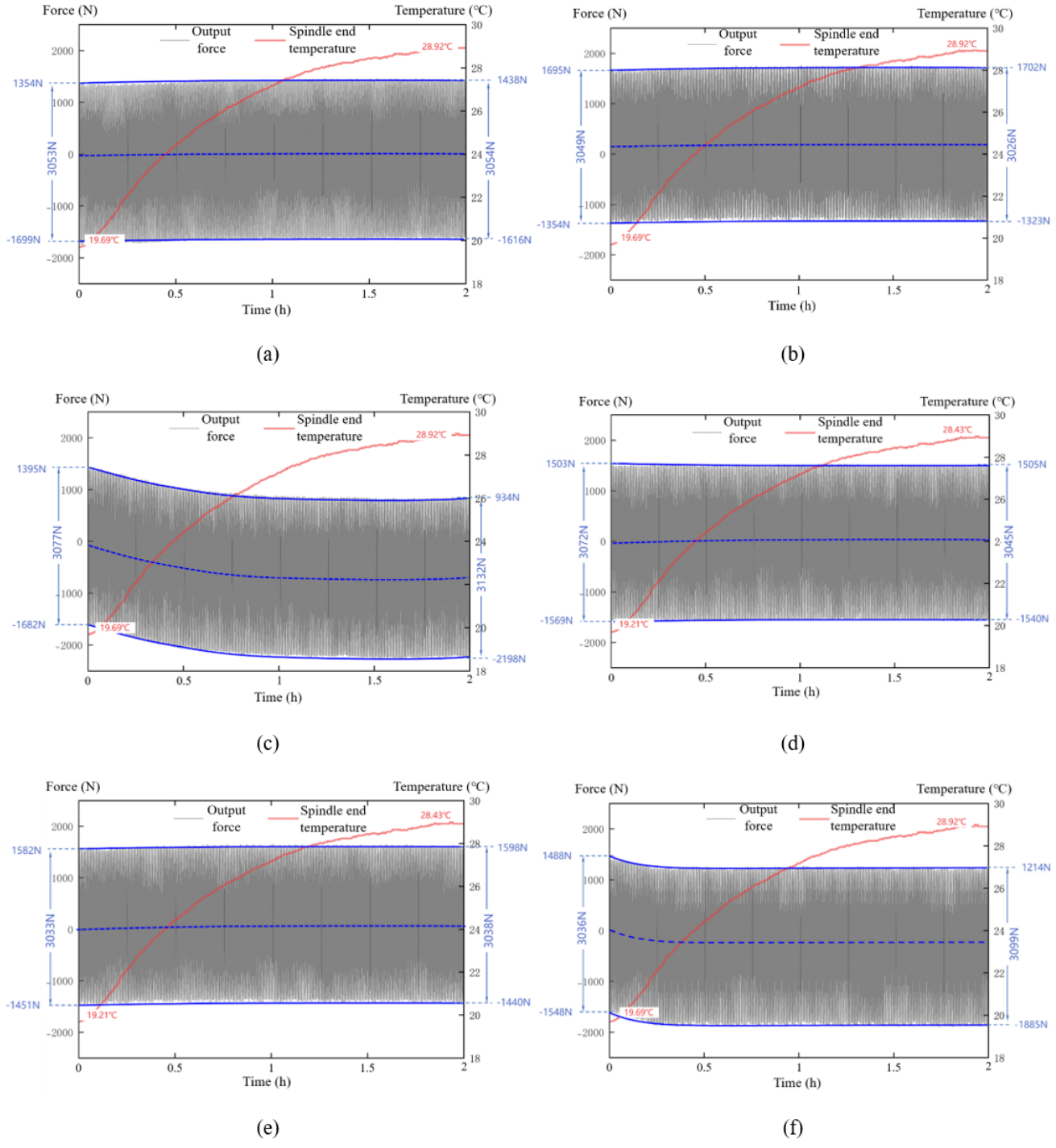

Figure 12. Loading device output force vs. temperature variation. **(a)** Dynamics-based feedforward control in the X direction. **(b)** Dynamics-based feedforward control in the Y direction. **(c)** Dynamics-based feedforward control in the Z direction. **(d)** BP-GA model predictive control in the X direction. **(e)** BP-GA model predictive control in the Y direction. **(f)** BP-GA model predictive control in the Z direction.

vice's loading capability and the practical applicability of BP-GA model predictive control.

The test has four steps. First, a Renishaw XM-60 multi-axis calibrator measures geometric accuracy over the full travel ranges of the X, Y, and Z axes to establish the initial accuracy baseline. Second, the loading device is installed, dynamic loads are applied in all three directions, and the spindle is operated at the specified speed. Third, after each loading cycle, the geometric accuracy of the machine tool is re-measured the following day. Fourth, upon completing the

Table 3. Comparison of three-direction force-tracking RMSEs between the two control methods under different operating conditions.

Loading frequency amplitude f (Hz)	Loading-force A(N)	Spindle speed n ($r\,min^{-1}$)	X-directional RMSE (N)		η_{RMSE} (%)	Y-directional RMSE (N)		η_{RMSE} (%)	Z-directional RMSE (N)		η_{RMSE} (%)
			Dynamics-based feedforward control	BP-GA model predictive control		Dynamics-based feedforward control	BP-GA model predictive control		Dynamics-based feedforward control	BP-GA model predictive control	
5	500	4000	12.3	10.2	17.1	30.0	24.2	19.3	84.3	28.4	66.3
5	1000	4000	21.3	14.9	30.0	50.7	30.0	40.8	107.3	42.5	60.4
5	2000	2000	34.4	21.4	37.8	86.2	33.4	61.3	146.2	121.8	16.7
5	2000	4000	35.6	21.0	41.0	85.4	35.2	58.8	162.4	119.4	26.5
5	2000	6000	48.4	21.6	55.4	131.6	25.6	80.5	227.5	124.6	45.2
10	500	4000	26.4	20.4	22.7	47.9	20.0	58.2	115.1	36.8	68.0
10	1000	4000	37.5	23.7	36.8	109.7	32.7	70.2	174.3	50.8	70.9
10	1500	4000	59.9	27.5	54.1	160.8	63.8	60.3	228.8	87.8	61.6
10	2000	4000	83.4	26.6	68.1	194.6	77.6	60.1	267.6	136.4	49.0
15	500	4000	36.6	22.0	39.9	75.4	26.1	65.4	138.6	48.7	64.9
15	1000	4000	54.4	38.8	28.7	131.2	62.7	52.2	178.3	78.0	56.3

Note that $\mathrm{RMSE} = \sqrt{\left[\frac{1}{N}\sum_{i=1}^{N}(F_{m,i} - F_{e,i})^2\right]}$, where N is the total number of sampling points included in the statistics, and $F_{m,i}$ and $F_{e,i}$ are the measured and desired output forces at the ith sampling point, respectively, and their difference is the force-tracking error, in N; $\eta_{RMSE} = (RMSE_{FF} - RMSE_{BP\text{-}GA})/RMSE_{FF} \times 100\,\%$, where η_{RMSE} is the RMSE reduction rate, and $RMSE_{FF}$ and $RMSE_{BP\text{-}GA}$ are the RMSEs of the dynamics model feedforward control and the BP-GA model predictive control under the same operating conditions, respectively.

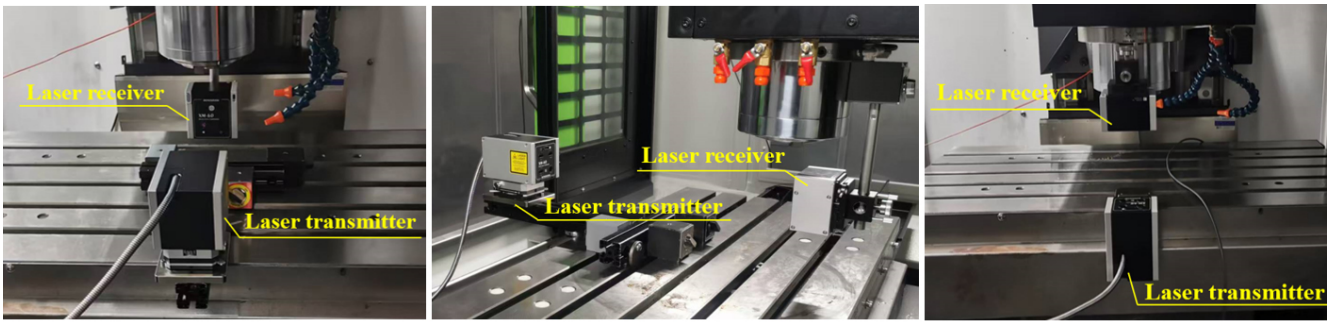

Figure 13. Experimental setup for geometric accuracy measurement. **(a)** X-axis geometric accuracy measurement setup. **(b)** Y-axis geometric accuracy measurement setup. **(c)** Z-axis geometric accuracy measurement setup.

specified cycles of on-machine loading and accuracy tests, all geometric accuracy data are statistically analyzed. The measurement setup is shown in Fig. 13.

Based on design parameters such as feed resistance and ultimate load capacity, together with engineering experience, the loading conditions are set to forces of 1000 N in X and Y and 1500 N in Z, a loading frequency of 10 Hz, and a spindle speed of 4000 $r\,min^{-1}$. Each loading cycle comprises 10 $h\,d^{-1}$ for 3 consecutive days, totaling 30 h. Each geometric accuracy measurement takes one day, and the complete experiment lasts 25 d.

Geometric accuracy is measured seven times during the experiment. The measurements cover six straightness errors and nine angular errors across the three axes, giving 15 geometric error components in total. The data are plotted in Fig. 14.

Based on multiple rounds of loading tests and geometric accuracy measurements, the following conclusions can be drawn:

1. Applying dynamic forces while rotating the spindle has an observable effect on machine tool geometric accuracy, demonstrating that the loading device can induce changes in accuracy.

2. The geometric error components exhibit different patterns. Some straightness errors show signs of a gradual increase, while angular errors remain generally stable. This suggests that dynamic loads may affect different geometric error components through different mechanisms.

3. The statistical analysis indicates that changes in geometric accuracy during the observation period are dominated by random fluctuations, with preliminary signs

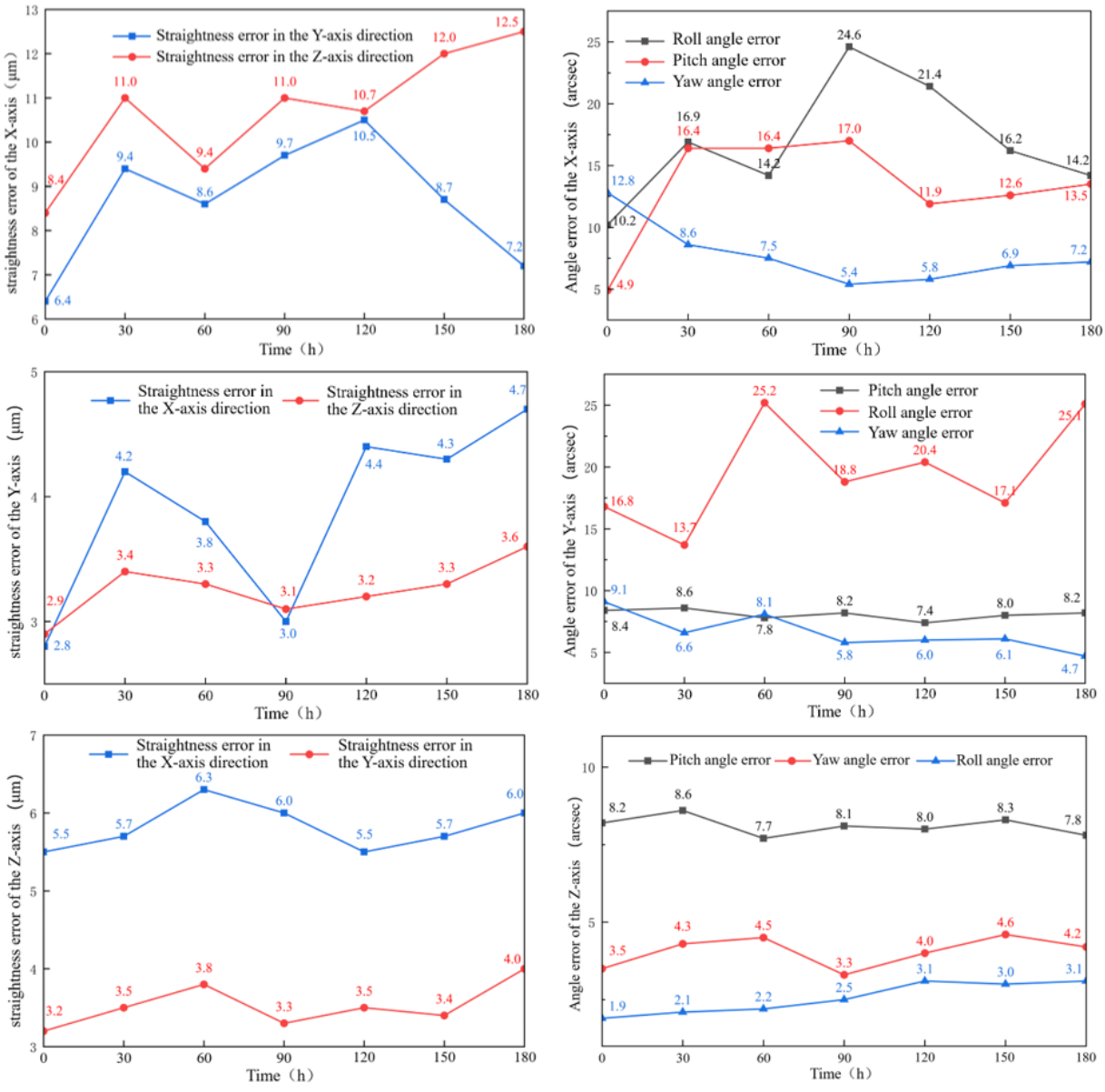

Figure 14. Geometric accuracy data curve.

of a gradual increase in some straightness errors. The limited test duration does not permit a definitive conclusion about long-term degradation trends. Longer observations are needed to investigate the degradation mechanisms.

4. The on-machine loading test with simulated cutting forces validates the device's loading capability and the effectiveness of the control method, providing an experimental basis for further accuracy retention testing and investigation of machine tool accuracy degradation mechanisms.

6 Conclusions

1. A compact 3-DOF on-machine loading device is developed based on a Delta parallel mechanism. It consists of a base platform, electric cylinders, rigid hinges, a moving platform, a three-dimensional force sensor, and an end effector. It applies dynamic loads simultaneously in X, Y, and Z and fits within the limited workspace inside a machine tool.

2. Forward and inverse kinematic models and a dynamic model are established and used to develop a dynamics-based feedforward controller. A BP-GA model predictive control method is further proposed to compensate for output-force deviations caused by spindle thermal deformation.

3. Comparative experiments show that BP-GA model predictive control reduces initial force-tracking errors relative to dynamics-based feedforward control, keeping the relative errors within 5 % in all three directions. It also reduces mean force deviations at thermal equilibrium, particularly the Z-direction force drift most affected by spindle thermal deformation. Across different loading frequencies, force amplitudes, and spindle speeds, BP-GA reduces RMSE by approximately 30 %–70 % under most conditions, demonstrating good tracking accuracy and adaptability to operating conditions.

4. Staged on-machine loading tests with simulated cutting forces are conducted. Within the observation period, changes in geometric errors are dominated by random fluctuations, although some straightness errors show signs of a gradual increase. The tests demonstrate the feasibility of the device and control method for on-machine loading with simulated cutting forces and provide a basis for accuracy retention testing.

5. Future work will validate static force output performance; compare the proposed method with other established force control methods; and combine longer-term, repeated accuracy measurements with measurement uncertainty analysis to investigate the evolution of machine tool accuracy and degradation mechanisms under dynamic loading.

Data availability. Data supporting this study's findings are available from the corresponding author upon reasonable request. These datasets are not publicly archived to protect ongoing research activities.

Author contributions. HL: conceptualization, methodology, investigation, formal analysis. MH: investigation, formal analysis, writing (review and editing). JX: software, writing (review and editing). HY: investigation, data curation. WH: validation, writing (review and editing). KL: conceptualization. DG: supervision.

Competing interests. The contact author has declared that none of the authors has any competing interests.

Disclaimer. Publisher's note: Copernicus Publications remains neutral with regard to jurisdictional claims made in the text, published maps, institutional affiliations, or any other geographical representation in this paper. The authors bear the ultimate responsibility for providing appropriate place names. Views expressed in the text are those of the authors and do not necessarily reflect the views of the publisher.

Review statement. This paper was edited by Pengyuan Zhao and reviewed by two anonymous referees.

References

Archenti, A., Nicolescu, M., Casterman, G., and Hjelm, S.: A New Method for Circular Testing of Machine Tools Under Loaded Condition, Proc. CIRP, 1, 575–580, https://doi.org/10.1016/j.procir.2012.05.002, 2012.

Cavus, M. and Allahham, A.: Enhanced Microgrid Control through Genetic Predictive Control: Integrating Genetic Algorithms with Model Predictive Control for Improved Non-Linearity and Non-Convexity Handling, Energies, 17, 4458, https://doi.org/10.3390/en17174458, 2024.

Ding, Z., Yang, Z., Chen, C., Chen, W., Chen, H., and Liu, Z.: Improved sliding mode dynamic matrix control strategy: Application on spindle loading and precision measuring device based on piezoelectric actuator, Mech. Syst. Signal Process., 167, 108543, https://doi.org/10.1016/j.ymssp.2021.108543, 2022.

Feng, L., Zhang, W., Gong, Z., Lin, G., and Liang, D.: Developments of Delta-Like Parallel Manipulators-A Review, Robot, 36, 375–384, https://doi.org/10.3724/SP.J.1218.2014.00375, 2014.

Guo, J., Wang, D., Chen, W., and Fan, R.: Multi-axis Loading Device for Reliability Tests of Machine Tools, IEEE/ASME Trans. Mechatron., 23, 1930–1940, https://doi.org/10.1109/TMECH.2018.2841883, 2018a.

Guo, J., Wang, D., Li, T., Gao, S., Chen, W., and Fan, R.: Triaxial loading device for reliability tests of three-axis machine tools, Robot. Comput.-Integr. Manuf., 49, 398–407, https://doi.org/10.1016/j.rcim.2017.05.009, 2018b.

Liu, H., Fan, R., Guo, J., Zhang, W., Zhao, Q., and Chen, W.: Multi-axis Loading Device for Reliability Tests of CNC Machine Tools, China Mech. Eng., 31, 1606–1612, https://doi.org/10.3969/j.issn.1004-132X.2020.13.013, 2020.

Lufinka, A.: Testing Device for Biaxial Loading of Textile Specimens, in: Proceedings of the 61st International Conference of Machine Design Departments (ICMD 2020), Košice, Slovakia (online), 2 December 2021, 23–32, https://doi.org/10.2991/978-94-6463-182-1_4, 2023.

Ma, J., Zhao, W., and Zhang, G.: Research Status and Analyses on Accuracy Retentivity of Domestic CNC Machine Tools, China Mech. Eng., 26, 3108–3115, https://doi.org/10.3969/j.issn.1004-132X.2015.22.020, 2015.

Ma, Z., Hu, X., and Zhou, Y.: Cross-Shaped Peg-in-Hole Autonomous Assembly System via BP Neural Network Based on Force/Moment and Visual Information, Machines, 12, 846, https://doi.org/10.3390/machines12120846, 2024.

Nelson, W. B.: Accelerated Testing: Statistical Models, Test Plans, and Data Analysis, Wiley Series in Probability and Statistics, John Wiley & Sons, New York, ISBN 978-0-471-69736-7, 2004.

San, H., Yang, X., Chen, J., Wu, X., Zhang, H., and Xu, B.: Kinematic Performance Analysis and Structural Parameter Optimiza-

tion of Delta Parallel Robot, Trans. Chin. Soc. Agric. Mach., 55, 446–458, https://doi.org/10.6041/j.issn.1000-1298.2024.08.042, 2024.

Sato, N., Izumi, K., and Iiduka, H.: Scaled Conjugate Gradient Method for Nonconvex Optimization in Deep Neural Networks, J. Mach. Learn. Res., 25, 1–37, https://jmlr.org/papers/v25/22-0815.html (last access: 19 November 2026), 2024.

Shang, D., Huang, X., Huang, Y., and Zhang, T.: Research on Rigid-flexible Coupling Dynamics of Delta Parallel Robot Based on Kane Equation, J. Mech. Eng., 60, 124–133, https://doi.org/10.3901/JME.2024.07.124, 2024.

Wang, J., Zhao, Y., Zhang, X., Li, Z., and Yao, W.: Model-Free Intelligent Control for Space Soft Robotic Manipulators, Space: Science & Technology, 4, 0120, https://doi.org/10.34133/space.0120, 2024.

Wang, Y., Wu, J., Liu, K., Liu, H., Liu, Z., and Lian, M.: Quantitative Evaluation and Error Sensitivity Analysis of Accuracy Retentivity of CNC Machine Tools, J. Mech. Eng., 55, 130–136, https://doi.org/10.3901/JME.2019.05.130, 2019.

Xu, G. and Huang, X.: Modeling and Characterization of Static and Dynamic Electromagnetic Forces of a Non-contact Electromagnetic Loading System, in: 2023 7th International Conference on Automation, Control and Robots (ICACR), Kuala Lumpur, Malaysia, 4–6 August 2023, 117–121, https://doi.org/10.1109/ICACR59381.2023.10314634, 2023.

Yang, Y., Zhang, K., Chen, Z., and Li, B.: Distributionally robust model predictive control for constrained robotic manipulators based on neural network modeling, Appl. Math. Mech.-Engl., 45, 2183–2202, https://doi.org/10.1007/s10483-024-3191-6, 2024.

Zhai, G., Chang, H., Liu, Z., Cai, C., Wang, Y., Wang, L., and Sun, R.: Development of 6-DOF Vibration Calibration System Based on Direct Drive Parallel Manipulator, Trans. Chin. Soc. Agric. Mach., 55, 414–423, 433, https://doi.org/10.6041/j.issn.1000-1298.2024.06.042, 2024.

Zhang, S., Ran, Y., Zhang, G., Murphy, A., and Li, X.: Quantitative Evaluation of Accuracy Retentivity and Analysis of Accuracy Degradation Mechanism, J. Mech. Eng., 58, 193–213, https://doi.org/10.3901/JME.2022.07.193, 2022.

Zhao, D., Zhang, G., and Dai, S.: Force servo controller design of electric control loading system, in: 2016 2nd International Conference on Control Science and Systems Engineering (ICCSSE), Singapore, 27–29 July 2016, 93–97, https://doi.org/10.1109/CCSSE.2016.7784360, 2016a.

Zhao, J., Wang, Z., Yang, T., Xu, J., Ma, Z., and Wang, C.: Design of a novel modal space sliding mode controller for electro-hydraulic driven multi-dimensional force loading parallel mechanism, ISA Trans., 99, 374–386, https://doi.org/10.1016/j.isatra.2019.09.018, 2020.

Zhao, W., Zhang, X., Lu, D., and Zhang, J.: Technical Status and Strategies for Domestic CNC Machine Tools, Aeronautical Manufacturing Technology, 59, 16–22, https://doi.org/10.16080/j.issn1671-833x.2016.09.016, 2016b.

Zhu, M., Huang, C., Song, S., Xu, S., and Gong, D.: Vision-admittance-based adaptive RBFNN control with a SMC robust compensator for collaborative parallel robots, J. Frankl. Inst., 361, 106538, https://doi.org/10.1016/j.jfranklin.2023.11.048, 2024.